

Towards controlled synthesis and better understanding of blue shift of the CaS crystals†

Cite this: *J. Mater. Chem. C*, 2014, 2, 2743

Cristiane W. Raubach,^{*a} Amanda F. Gouveia,^a Yuri V. B. de Santana,^{ab} José A. Varela,^b Mateus M. Ferrer,^a Maximo S. Li^c and Elson Longo^b

For the first time, the calcium sulfide (CaS) photoluminescent (PL) emission blue shift synthesized by the microwave-assisted solvothermal (MAS) method was examined to understand its key role in the PL activity. PL emission in the visible region showed a blue shift with synthesis time variations. In addition, we also investigated the electronic structure using first-principles calculations based on density functional theory (DFT) which was applied to periodic models at the B3LYP level. Two models were selected to simulate the effects of structural deformation on the electronic structure: (1) the ordered model (*o*-CaS) and (2) the disordered model (*d*-CaS). This PL emission shift is linked to distortions and defects which generate modifications in the electronic states and facilitate the possibility of numerous decay transactions to the valence band (VB).

Received 25th October 2013
Accepted 28th January 2014

DOI: 10.1039/c3tc32115k

www.rsc.org/MaterialsC

Introduction

Sulfide phosphors such as ZnS, SrS and CaS have properties which are useful for practical applications such as: television screens, fluorescent lamps, thermoluminescent dosimeters, X-ray imaging screens and high pressure mercury lamps.^{1–5}

In the past decades, alkaline earth sulfides (AES) have received considerable attention.^{6–8} Members of this group also are known as wide band-gap semiconductors (*e.g.*, CaS 3.4–4.4 eV, MgS 5.27–5.47 eV and SrS 4.3 eV). Among these semiconductors CaS has been actively studied.^{9,10} CaS is known as an afterglow phosphor with high luminescent efficiency and multiple luminescent centers. CaS exhibits luminescence under irradiation at various wavelengths of light, X-rays, ultraviolet and visible light.^{11–13}

CaS can crystallize into four different structures: (1) NaCl-type (B1); (2) CsCl-type (B2); (3) zinc-blende (B3); (4) wurtzite (B4).^{14,15} At room temperature, CaS crystallizes into a NaCl structure (rock-salt) which is cubic ($Fm\bar{3}m$) with atoms occupying octahedral sites. Calcium cations are arranged in an fcc (face-centered cubic) pattern, and sulfur anions reside in the octahedral holes (see, Fig. 1). Each calcium or sulfur atom is surrounded by six atoms of the opposite kind which results in a coordination expressed as (6 : 6).

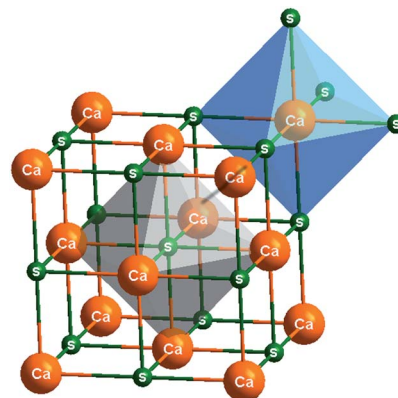


Fig. 1 Arrangement of calcium and sulfur atoms in the CaS structure.

The structure, morphology and density of defects are crucial factors in determining optical and electronic properties of these materials.^{16,17} Thus, one of the most important goals in modern materials research is the development of simple and low cost methods for large scale synthesis, as well as an understanding of the structure, shape and density of defects generated by the method employed.

In this respect, very little research has been reported on the preparation of CaS nanoparticles with and without dopants such as: co-precipitation for CaS:Eu²⁺, an alkoxide method for CaS,^{2,18} a solvothermal method for CaS and SrS⁹ and a microwave heating method for CaS.¹⁹

Microwave-assisted solvothermal synthesis has been extensively employed in recent years for powder field preparation due to important benefits such as, kinetic enhancement, low reaction temperature, time reduction and relative control of sizes and shapes.^{20–22}

^aCDMF/INCTMN-UFSCar, Universidade Federal de São Carlos, Rod. Washington Luís Km 235, 13565-905, São Carlos, SP, Brazil. E-mail: cristiane@lic.ufscar.br

^bCDMF/INCTMN-UNESP, Universidade Estadual Paulista, P.O. Box 355, 14801-907, Araraquara, SP, Brazil

^cIFSC-Universidade de São Paulo, P.O. Box 369, 13560 970, São Carlos, SP, Brazil

† Electronic supplementary information (ESI) available. See DOI: 10.1039/c3tc32115k

This study focuses on links between the structure and the photoluminescent behavior of calcium sulfide. We investigate the role of microwave processing on the photoluminescent properties of CaS crystals. The main objective is to investigate the impact of order–disorder on PL emission. This research involves two steps: (1) powder synthesis at different times and (2) revealing relationships between structural disorder and the PL property. The purpose is to combine both experimental and theoretical results to explain PL emission response at room temperature and the structure order–disorder relationship using the cluster-to-cluster-charge-transfer (CCCT) concept.²³ Thus, in this study, different experimental techniques and calculations based on DFT were employed to conduct a comprehensive investigation of corresponding structures and electronic properties.

Experimental

Preparation of calcium sulfide crystals

4 mmol of $\text{Na}_2\text{S} \cdot 9\text{H}_2\text{O}$ (99%, Synth) was dissolved in 75 mL of ethanol. 300 mL min^{-1} of N_2 gas was insufflated into this solution for 30 min (solution 1). In a separate step, 4 mmol of CaCl_2 (99.90%, Synth) was dissolved in 75 mL of ethanol (solution 2). Then solutions 1 and 2 were mixed in a 120 mL Teflon autoclave; after 10 min the precipitate was placed in the microwave system at 110 °C for different times (4–64 min). The resulting solution was washed with tetrahydrofuran (THF) (99.5%, Merck) several times to neutralize the solution pH (≈ 7), and the precipitates were finally collected and dried at 70 °C (5 h).

Characterization

The powders obtained were structurally characterized by X-ray diffraction (XRD) patterns using a D/Max-2500PC diffractometer (Rigaku, Japan) with Cu $K\alpha$ radiation ($\lambda = 1.5406 \text{ \AA}$) in the 2θ range from 20° to 75° in the normal routine with a scanning velocity of 2° min^{-1} and from 10° to 110° with a scanning velocity of 1° min^{-1} . CaS crystal shapes and sizes were observed with a field-emission scanning electron microscope (FE-SEM, Zeiss Supra™ 35 model) operating at 10 kV. Ultraviolet-visible (UV-vis) spectra were recorded using a Varian spectrophotometer (Cary 5G model) in a diffuse-reflectance mode. PL measurements were performed using a Monospec 27 monochromator (Thermal Jarrel Ash) coupled to a R446 photomultiplier (Hamamatsu Photonics, Japan). A Kr-ion laser (Coherent Innova 90 K; $\lambda = 350.0 \text{ nm}$) was used as the excitation source with the output power maintained at 500 mW. The laser beam was passed through an optical chopper and its maximum power on the sample was maintained at 40 mW. All measurements were taken at room temperature.

Computational method and CaS crystal periodic model

The simulation was performed using a periodic approximation as implemented in the CRYSTAL09 computer code.²⁴ The computational method is based on DFT in conjunction with Becke's three-parameter hybrid non-local exchange functional²⁵ combined with

the Lee–Yang–Parr gradient-corrected correlation functional, B3LYP.²⁶ Atomic centers for Ca and S atoms have been described by all electron basis sets 86-511d3G and 86-311G*, respectively, provided by the CRYSTAL basis sets library.²⁷

As a first step, an optimization procedure of the lattice parameter a from the experimental value of 5.65 Å was completed which yielded an a value of 5.76 Å. From these optimized parameters, periodic models with a 16-atom supercell CaS (Ca_8S_8) were built: (1) the orderly CaS model (o -CaS); and (2) the disorderly CaS model (d -CaS) where the S atom was displaced which simulates defects that can occur experimentally in the structure. This strategy was used in previous studies.^{28–35} The purpose of this procedure is to explain observed differences in experimental samples' band gaps.

Results and discussion

Fig. 2 depicts XRD patterns for CaS crystals prepared by the MAS method for different times. XRD patterns indicate that all CaS crystals have a cubic structure without any deleterious phases with a space group of $Fm\bar{3}m$ (225). These crystals have a sharp and well defined diffraction peak which indicates a reasonable degree of structural order and crystallinity at long range. Moreover, all diffraction peaks are in good agreement with the respective Inorganic Crystal Structure Data (ICSD) base no. 41956 (ref. 36) and the literature.^{6,37}

According to Chen,¹⁵ CaS crystals can exhibit polymorphism: this sulfide can have different structures such as: NaCl-type (B1), CsCl-type (B2), zinc blende (B3), and wurtzite (B4). The NaCl structure is stable under ambient conditions and the CsCl structure is stable above 45 GPa.³⁸ Rietveld refinement was performed based on the CaS phase with a cubic structure (B1) using better approximation and indexing of the crystallographic information file (CIF) and employing CIF 41956.³⁶ Fig. S1† confirms that there is good agreement between experimentally observed XRD patterns and theoretically fitted results which

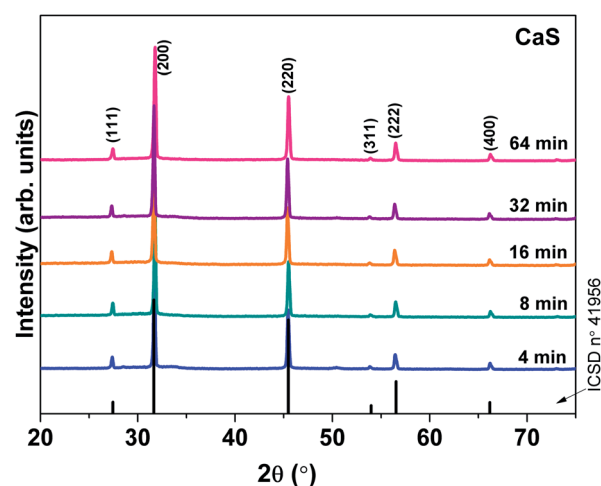


Fig. 2 XRD patterns of CaS crystals synthesized by MAS for different times. The vertical lines indicate the position and relative intensity of the ICSD card no. 41956 (ref. 36) for the cubic CaS phase.

indicates the success of the Rietveld refinement method (see Table S1 and Fig. S1 in the ESI†).

The optical band-gap energy (E_{gap}) was calculated by the method proposed by Kubelka and Munk-Aussing.³⁹ This methodology is based on the transformation of diffuse-reflectance measurements to estimate E_{gap} values with good accuracy within the limits of assumptions when modeled in three dimensions.⁴⁰ The Kubelka–Munk equation for any wavelength is described as

$$F(R_{\infty}) = \frac{(1 - R_{\infty})^2}{2R_{\infty}} = \frac{K}{s} \quad (1)$$

where $F(R_{\infty})$ is the Kubelka–Munk function or the absolute reflectance of the sample. $R_{\infty} = R_{\text{sample}}/R_{\text{standard}}$ (R_{∞} is the reflectance when the sample is infinitely thick), κ is the molar absorption coefficient, and s is the scattering coefficient. In a parabolic band structure, the optical band gap and absorption semiconductor coefficient⁴¹ can be calculated by the following equation:

$$\alpha h\nu = C_1(h\nu - E_{\text{gap}})^n \quad (2)$$

where α is the linear absorption coefficient of the material, $h\nu$ is the photon energy, C_1 is a proportionality constant, E_{gap} is the optical band gap, and n is a constant associated with different kinds of electronic transitions ($n = 0.5$ for a direct allowed and $n = 2$ for an indirect allowed). Chen *et al.*¹⁵ conducted a theoretical study regarding structural and electronic properties of the CaS compound by considering four phases (B1, B2, B3 and B4). Their theoretical studies show that the B1 phase (NaCl-type) of CaS has a direct band gap. However, Kaneco and Koda⁴² claimed that the CaS band gap in B1 phases is governed by indirect transitions between the VB and conduction bands (CB) due to the lower transition energy with values of 4.4 eV. Based on experimental data, our theoretical models demonstrate that CaS has a direct electronic transition occurring at the Γ point of the Brillouin zone. Thus, E_{gap} CaS crystals values were calculated using eqn (2) for a direct allowed transition.

Charge carriers produced by the MAS synthesis in the CaS form localized polaronic states, due to bond distortion, interface intrinsic defects and sulfur vacancies. These polarons can undergo different trappings or recombination processes. This excited state favors the population of intermediary energy levels within the band gap. The sulfur displacement related to the Ca, modulates these different species of trapped electrons and holes.

Fig. 3 shows the plot of the optical band gap values for the structures which are experimentally and theoretically studied: *o*-CaS and *d*-CaS with a displacement in the *z*-axis: 0.1, 0.3 and 0.5 Å. The increase of the defect caused by the displacement of the sulfur atom in the *z*-axis decreases E_{gap} values. The decrease in the experimentally obtained E_{gap} values can be explained according to the time that the solution remained in the microwave system. In the system, parts of the material can crystallize, dissolve and recrystallize several times.⁴³ This recrystallization process leads to modifications in the structural order which is directly linked to material electronic levels and is the reason for breaking the variation tendency of the estimated band gap after a long time in the microwave (64 min).

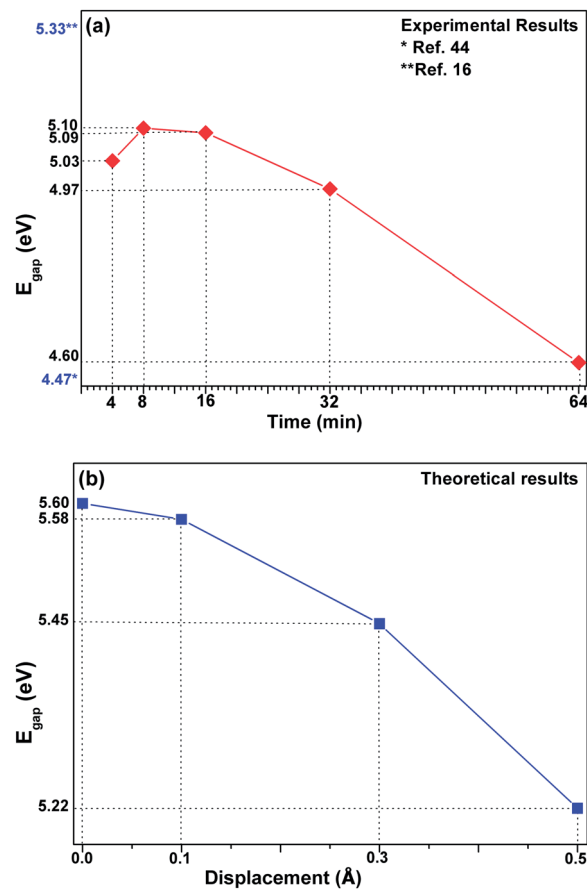


Fig. 3 (a) Experimental and (b) theoretical band gap values (eV) for CaS.

For CaS in B1 phases, we have found a direct band gap between the top of S 3p valence bands occurring at the Γ point and the bottom of the Ca 3d bands occurring at the same point, confirming the previous results found by Chen *et al.*¹⁵ and contradict to the results obtained by others.^{14,42}

Total density of states (TDOS) and partial density of states (PDOS) obtained by first principles calculations for *o*-CaS and *d*-CaS are shown in Fig. 4.

TDOS and PDOS are very useful to verify different transition location levels and band compositions.

Regarding TDOS, the displacement of the sulfur atom in the system generated a considerable modification of the profile. TDOS of the *d*-CaS (0.0 0.0 0.1) is not shown in Fig. 4 due to its similarity to *o*-CaS.

PDOS projected on the atoms indicates that the valence band (VB) maximum is derived mainly from S p orbitals with a minor contribution of Ca 3d ($3d_{z^2}$ and $3d_{x^2-y^2}$) orbitals. Thus, the hybridization in CaS is sp^3d^2 (s and p-orbitals from S and d-orbitals from Ca) that characterize an octahedral structure. For the conduction band (CB) region, PDOS shows that this region is predominantly derived from Ca 3d orbitals with a minor contribution of s and p orbitals from S. Ca 3d orbitals are composed of two arrangements of hybrid orbitals: the first orbital is formed of Ca $3d_{xz}$, $3d_{yz}$ and $3d_{xy}$ while the second

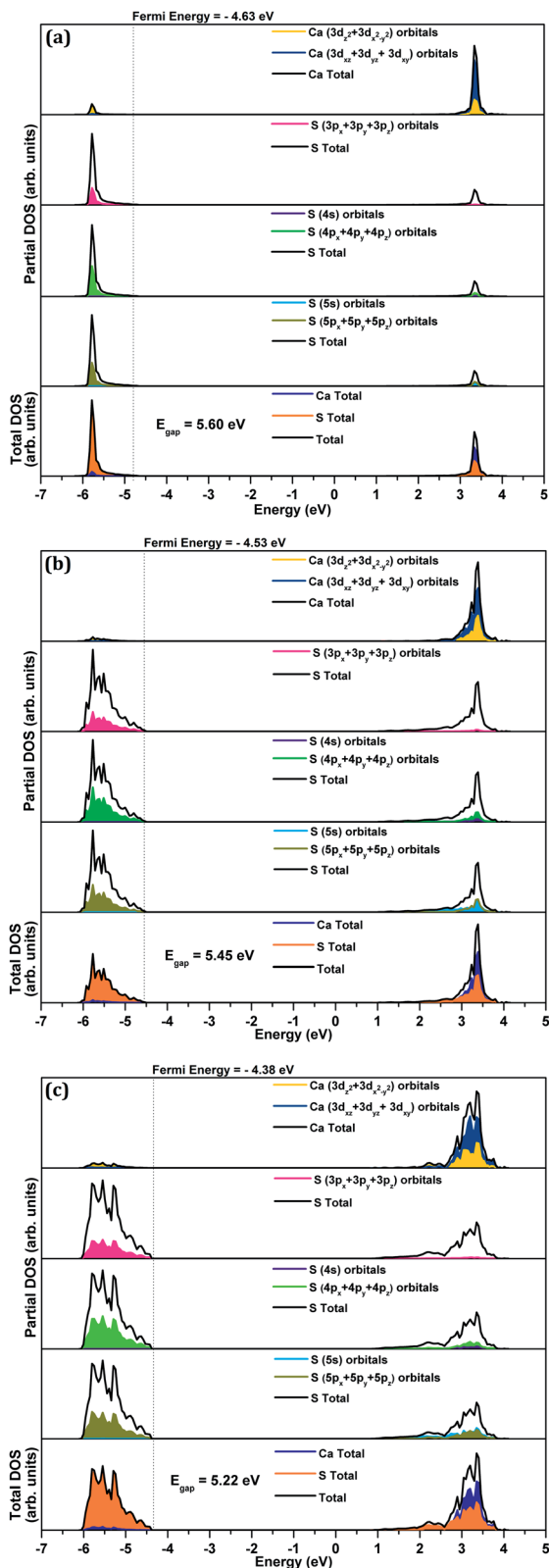


Fig. 4 Partial DOS and total DOS projected in: *o*-CaS (a), *d*-CaS: (b) (0.0 0.0 0.3) and (c) (0.0 0.0 0.5).

orbital is constituted of Ca $3d_{x^2-y^2}$ and $3d_{x^2-y^2}$, with a higher contribution of Ca $3d_{xz}$, $3d_{yz}$ and $3d_{xy}$ than Ca $3d_{z^2}$ and $3d_{x^2-y^2}$ orbitals. By analyzing the VB and CB in more detail, it was

possible to construct Table 1 where the percent of contributions of the atomic orbitals (AO) from Ca and S are shown.

There is a decrease in bonding orbital contributions in *d*-CaS models and an increase in anti-bonding orbitals. Thus, the defect contributes to an increase in the anti-bonding orbital levels which result in a higher probability of finding electrons in this region. These electrons in anti-bonding orbitals create a polarization in $[\text{CaS}_6]$ clusters. This displacement induces structural distortions in the octahedron which simultaneously and directly affects the conduction and valence regions. Quantum mechanical calculations of *d*-CaS indicate that localized states generated in the band gap region reduce gap energies. These results confirm the disorganization of the lattice that generates new states in the PDOS.

Fig. 5 illustrates FE-SEM images of CaS crystals obtained at different synthesis times. Particles are agglomerated with no

Table 1 Contributions of AO to DOS from Ca and S

Model	Atom	Contributions (%)		
		VB	CB	Clusters
<i>o</i> -CaS	Ca	5.2	60.5	$[\text{CaS}_6 \cdot V_S^0]$
	S	94.8	39.5	
<i>d</i> -CaS (0.0 0.0 0.1)	Ca	4.8	60.1	$[\text{CaS}_5 \cdot V_S^{\pm}]$
	S	95.2	39.9	
<i>d</i> -CaS (0.0 0.0 0.3)	Ca	4.3	59.6	$[\text{CaS}_5 \cdot V_S^{\pm}]$
	S	95.7	40.4	
<i>d</i> -CaS (0.0 0.0 0.5)	Ca	3.9	57.5	$[\text{CaS}_5 \cdot V_S^{\pm}]$
	S	96.1	42.5	

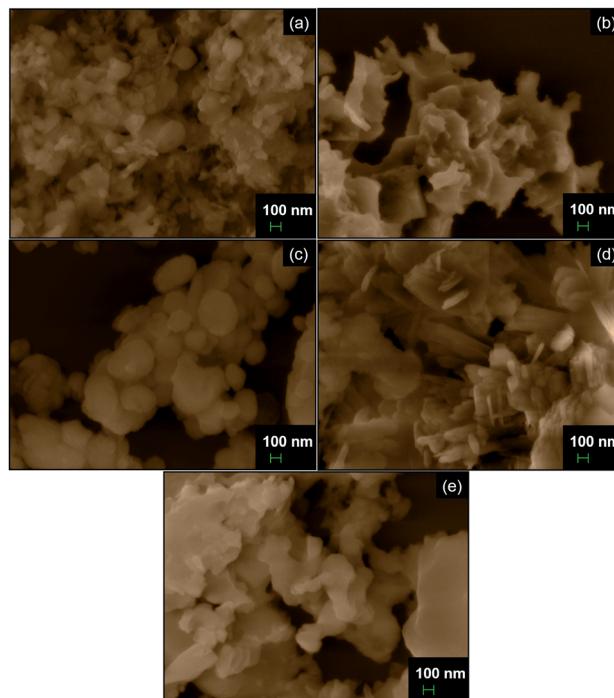


Fig. 5 FE-SEM images of CaS synthesized by the MAS method at (a) 4, (b) 8, (c) 16, (d) 32 and (e) 64 min.

specific morphology which possibly is due to the re-crystallization process. The general aspect of the sample morphology changes with synthesis time due to the agglomeration and lack of a specific morphology, it is impossible to obtain satisfactory statistics on particle sizes. However, they have different sizes ranging from ~ 100 nm (see Fig. 5c) up to several micrometers (see Fig. 5e).

Fig. 6 illustrates PL evolutions of CaS samples synthesized by a MAS method for different times. The profiles have a typical behavior of multiphonon or multilevel processes *i.e.*, a solid system where the relaxation occurs by several pathways, which involve the participation of numerous energy states within the band gap^{44,45} and originate from intrinsic defects of the material. In the photoluminescent response for CaS samples with a 350.7 nm excitation source, the luminescent behavior is composed of a broad luminescent band in the range of 350–650 nm which is centered around 450 nm in the blue-green region of visible spectra with two shoulders after and before the maximum emission. In general, PL emission spectra of CaS are frequently decomposed into blue and green light components. Wang *et al.* explained the green emission of the CaS crystals by the relatively lower temperature of the synthesis.³⁷ Jia *et al.* conducted a study comparing the doping with different ions (Na^+ , Tm^{3+} , and Bi^{3+}). They found that doping Na^+ ions could efficiently reduce the photoluminescent emission.⁴⁶ Kumar *et al.* investigated the effect of different dopant (Ce^{3+}) concentrations on the PL emission intensity. PL emission peaks of both Ce^{3+} ion transitions were blue-shifted from the normal PL of the bulk CaS.⁴⁷

In this study, the PL behavior is explained by photogenerated electron-hole pair (excitons) processes and in terms of the electronic transition between the VB (3p levels of S atoms) and the CB (3d levels of Ca atoms). These results confirm that structural defects in the CaS crystal lattice are responsible for the appearance of intermediate levels between the VB and CB which favor intense PL emission properties at room temperature. With crystallization evolution, the atomic crystalline design possesses a better electronic configuration that promotes PL emission.

First principles quantum mechanical calculations have shown that the break in the lattice symmetry due to structural

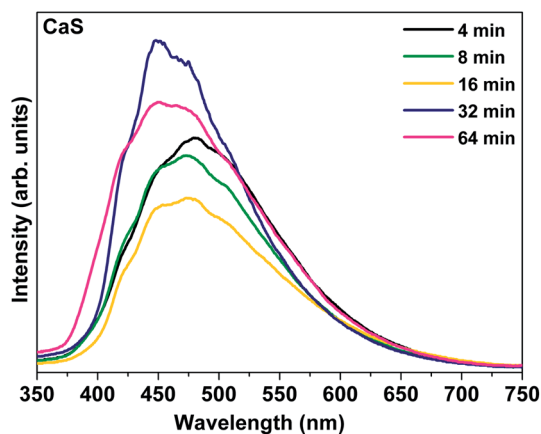


Fig. 6 PL emission spectrum of CaS synthesized by MAS for different times.

disorder is responsible for electronic states in the band gap and reveals that this disordered structure produces local polarization and a charge gradient in the structure. New levels are formed above the VB and below the CB which are associated with a specific CaS structural disorder.^{44,45,48,49}

The wide band model illustrated in Fig. 7a provides three necessary steps for a PL emission to occur: (1) in the first step, the excitation source, $h\nu$, corresponds to the energy to promote a photon absorption from S 3p states at the valence up to Ca 3d states inside the forbidden band gap; (2) after excitation, the recombination process occurs among the excited 3d states closer to the CB; and (3) a wide band PL emission due to allowed $3d \rightarrow 3p$ transitions, associated with a multiple $h\nu'$ energy, can be measured.

During the excitation process, the CCCT in a crystal containing more than one kind of cluster is characterized by excitations involving electronic transitions from one cluster to another cluster. Here there are two types of clusters for Ca or S atoms. Sulfur vacancies in a disordered structure with $[\text{CaS}_6]'/[\text{CaS}_5V_S^-]$ complex clusters are electron-trapping or hole-trapping centers, according to the following equations:

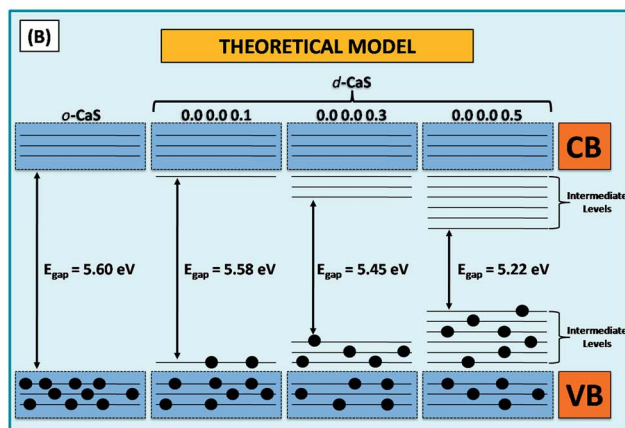
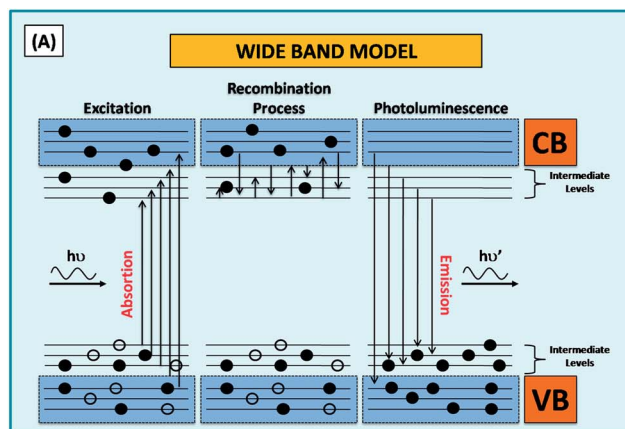


Fig. 7 (a) Wide band model to illustrate the three steps of PL emissions and (b) the theoretical model of CaS.

where, a $[\text{CaS}_6]$ donor, $[\text{CaS}_5 \cdot V_S^{\cdot-}]$ is a donor/acceptor and $[\text{CaS}_5 \cdot V_S^{\cdot+}]$ is an acceptor. It is assumed that charge redistribution may facilitate the electron-hole recombination of localized excitons. Structural and electronic reconstructions of all possible combinations of clusters belonging to a specific crystal are essential to understand the complex CCCT process and its influences on the PL phenomenon. This series of equations represents complex clusters in structural disordered solids and illustrates the sulfur vacancy occurrences that facilitate the interaction between interclusters.

The theoretical model in Fig. 7b is based on the wide band model to explain the creation of intermediate levels with a decrease in the band gap value. This model can be linked with the wide band model (see Fig. 7a) because of the different kinds of defect changes in band profiles which create new intermediate levels in the forbidden region.

Fig. 8 contains electron density maps for CaS crystals along the exposed edge in the (100) direction. The contour plot reveals that bonding between Ca and S has an ionic bonding nature. Note that there is no common isoline between Ca and S atoms; *i.e.* an isoline that contours both atoms. The S atom displacement generated a difference in the charge density of the lattice as expected. These displacements of the chemical bond of CaS cause the formation of a hole-electron in the region surrounding the defect. The electron is self trapped by sulfur and the hole is self trapped by calcium which is associated with polaronic distortion and is apparent when analyzing the atomic orbitals of atoms localized in the defect region. These results show that the electronic density is located in s and p orbitals (electron trap), and the d orbital has lower density electronics (hole trap). These displacements result in a kind of sulfur vacancy, and thus, more than one kind of cluster will exist in the structure, as $[\text{CaS}_6 \cdot V_S^0]$, $[\text{CaS}_5 \cdot V_S^{\cdot+}]$, $[\text{CaS}_5 \cdot V_S^{\cdot-}]$ and/or $[\text{CaS}_5 \cdot V_S^{\cdot-}]$.

The annealing time is important in determining photoluminescent particle properties.

The particle prepared by the microwave process has a high photoluminescent intensity which is achieved by annealing particles. Better photoluminescent properties were obtained after 32 min of synthesis. Varying the annealing time for CaS crystals produces shifts in photoluminescent spectra which indicates that the particle emission wavelength could be adjusted by changing the synthesis time.

For the PL profile displayed in Fig. 6, luminescent spectra are broken up into three peaks and each peak was fitted to a symmetric Gaussian function. Fig. 9 depicts typical peak resolution results as a function of time, which demonstrates that three Gaussian curves constitute overall luminescence in the visible region from approximately 350–650 nm and show the contribution of each deconvoluted curve and its variation. Upon deconvolution, three curves were chosen to describe emissions of 443 nm, 490 nm (blue components) and 549 nm (green components).

With an increase in the time synthesis up to 32 min, the contribution of the green region decreases and the blue region increases. In the 64 min sample, there is a low shift to the red direction that can be related to new defects created by the MAS method.



Fig. 8 Electron density maps for CaS crystals in the (100) direction: o-CaS (a), d-CaS: (b) (0.0 0.0 0.1), (c) (0.0 0.0 0.3) and (d) (0.0 0.0 0.5).

The contribution of each peak measured by its corresponding area can be separated into three different behaviors. The correspondent peak of the blue component (443 nm) increases from 18% to 50%, while the correspondent peak of the green component (549 nm) produces the opposite effect and decreases from 34% to 23% the same behavior occurs with the blue component (490 nm). Although the estimated band gap by the Wood-Tauc method did not show the same behavior in relation to the PL shift, it cannot be employed to explain all electron transitions responsible for the wide luminescent band. According to the wide band theory, distortions and defects generate modifications in the electronic states and provide the possibility of numerous decay transitions to the VB. For this reason, the result is a wide band of luminescence (a contribution of a large amount of wavelengths).⁴⁵

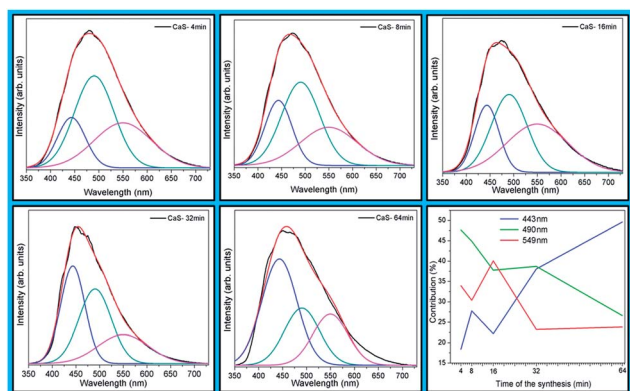


Fig. 9 Deconvoluted PL bands in three curves centered at 443 nm, 490 nm and 549 nm and their contributions.

Conclusions

In summary, for the first time, CaS crystals were successfully synthesized by the MAS method at a low temperature and a short time (4 min). XRD patterns show that CaS crystals have a NaCl-type cubic structure with a space group of $Fm\bar{3}m$. FE-SEM images reveal the formation of large aggregated crystals with different sizes and morphologies. Different E_{gap} values were attributed to localized electronic levels within the forbidden band gap which is caused by structure defects. Theoretical calculations indicate that band structures of all CaS models are characterized by direct electronic transitions. According to TDOS and PDOS analyses, energy states in the VB are constituted from S (3p) orbitals while energy states in the CB are from Ca (3d) orbitals with a small contribution from S (3d) orbitals. Increasing the synthesis time up to 32 min causes a blue shift in the maximum PL emission that can be attributed to the structural organization. As reported in the theoretical results, the organized (*o*-CaS) model showed a higher band gap than the other disorganized (*d*-CaS) models that can be correlated with experimental results: by increasing the synthesis time there is more organization in the system.

Acknowledgements

The authors are thankful for the financial support of Brazilian research financing institutions: CAPES, CNPq and FAPESP – 2010/19484-0, 2012/07967-1, 2012/22823-6 and 2012/14468-1.

Notes and references

- H. S. Bhatti, R. Sharma and N. K. Verma, *J. Mod. Opt.*, 2006, **53**, 2021–2031.
- H. S. Bhatti, R. Sharma and N. K. Verma, *Radiat. Eff. Defects Solids*, 2006, **161**, 113–119.
- S. Adhikary, A. Choubey, S. Das, S. K. Sharma and J. Manam, *J. Alloys Compd.*, 2010, **489**, 4–8.
- H. S. Bhatti, S. Singh, N. K. Verma and S. Kumar, *Indian J. Eng. Mater. Sci.*, 2002, **9**, 69–74.
- M. A. S. Sweet and J. Rennie, *Nucl. Instrum. Methods Phys. Res., Sect. A*, 1989, **283**, 330–334.
- W. Lehmann and F. M. Ryan, *J. Electrochem. Soc.*, 1971, **118**, 477.
- N. Sawada, Y. Chen and T. Isobe, *J. Alloys Compd.*, 2006, **408–412**, 824–827.
- V. Kumar, V. Mishra, M. M. Biggs, I. M. Nagpure, O. M. Ntwaeaborwa, J. J. Terblans and H. C. Swart, *Appl. Surf. Sci.*, 2010, **256**, 1720–1724.
- W. Z. Wang, I. Germanenko and M. S. El-Shall, *Chem. Mater.*, 2002, **14**, 3028–3033.
- G. Sharma, P. Chawla, S. P. Lochab and N. Singh, *Chalcogenide Lett.*, 2009, **6**, 705–712.
- J. E. Van Haecke, P. F. Smet and D. Poelman, *J. Lumin.*, 2007, **126**, 508–514.
- Y. Kojima, K. Aoyagi and T. Yasue, *J. Lumin.*, 2007, **126**, 319–322.
- J. E. Van Haecke, P. F. Smet, K. De Keyser and D. Poelman, *J. Electrochem. Soc.*, 2007, **154**, J278–J282.
- A. Shaukat, Y. Saeed, N. Ikram and H. Akbarzadeh, *Eur. Phys. J. B*, 2008, **62**, 439–446.
- Z. J. Chen, H. Y. Xiao and X. T. Zu, *Phys. B*, 2007, **391**, 193–198.
- T. Yamamoto, S. Kishimoto and S. Iida, *Phys. B*, 2001, **308–310**, 916–919.
- Z. F. Ding, B. M. Quinn, S. K. Haram, L. E. Pell, B. A. Korgel and A. J. Bard, *Science*, 2002, **296**, 1293–1297.
- B. Q. Sun, G. S. Yi, D. P. Chen, Y. X. Zhou and J. Cheng, *J. Mater. Chem.*, 2002, **12**, 1194–1198.
- P. J. Liu and Y. L. Liu, *Chin. Chem. Lett.*, 2000, **11**, 843–846.
- T. N. Glasnov and C. O. Kappe, *J. Chem. Neuroanat.*, 2011, **17**, 11956–11968.
- D. P. Volanti, D. Keyson, L. S. Cavalcante, A. Z. Simões, M. R. Joya, E. Longo, J. A. Varela, P. S. Pizani and A. G. Souza, *J. Alloys Compd.*, 2008, **459**, 537–542.
- M. L. Moreira, J. Andrés, J. A. Varela and E. Longo, *Cryst. Growth Des.*, 2009, **9**, 833–839.
- L. S. Cavalcante, V. M. Longo, J. C. Sczancoski, M. A. P. Almeida, A. A. Batista, J. A. Varela, M. O. Orlandi, E. Longo and M. Siu Li, *CrystEngComm*, 2012, **14**, 853–868.
- R. Dovesi, V. R. Saunders, C. Roetti, R. Orlando, C. M. Zicovich-Wilson, F. Pascale, B. Civalleri, K. Doll, N. M. Harrison, I. J. Bush, P. D'Arco and M. Llunell, *CRYSTAL09 User's Manual*, Torino, 2009.
- A. D. Beacke, *J. Chem. Phys.*, 1993, **98**, 5648–5652.
- C. T. Lee, W. T. Yang and R. G. Parr, *Phys. Rev. B: Condens. Matter Mater. Phys.*, 1988, **37**, 785–789.
- Crystal, http://www.crystal.unito.it/Basis_Sets/Ptable.html.
- P. G. Mendes, M. L. Moreira, S. M. Tebchrani, M. O. Orlandi, J. Andrés, M. Siu Li, N. Diaz-Mora, J. A. Varela and E. Longo, *J. Nanopart. Res.*, 2012, **14**, 750.
- M. R. D. Bomio, L. S. Cavalcante, M. A. P. Almeida, R. L. Tranquilin, N. C. Batista, P. S. Pizani, M. Siu Li, J. Andrés and E. Longo, *Polyhedron*, 2013, **50**, 532–545.
- L. S. Cavalcante, E. Moraes, M. A. P. Almeida, C. J. Dalmaschio, N. C. Batista, J. A. Varela, E. Longo,

- M. Siu Li, J. Andrés and A. Beltrán, *Polyhedron*, 2013, **54**, 13–25.
- 31 L. Gracia, V. M. Longo, L. S. Cavalcante, A. Beltrán, W. Avansi, M. Siu Li, V. R. Mastelaro, J. A. Varela, E. Longo and J. Andrés, *J. Appl. Phys.*, 2011, **110**, 043501.
- 32 L. Gracia, J. Andrés, V. M. Longo, J. A. Varela and E. Longo, *Chem. Phys. Lett.*, 2010, **493**, 141–146.
- 33 J. C. Sczancoski, L. S. Cavalcante, N. L. Marana, R. O. da Silva, R. L. Tranquilin, M. R. Joya, P. S. Pizani, J. A. Varela, J. R. Sambrano, M. Siu Li, E. Longo and J. Andrés, *Curr. Appl. Phys.*, 2010, **10**, 614–624.
- 34 V. M. Longo, L. S. Cavalcante, M. G. S. Costa, M. L. Moreira, A. T. de Figueiredo, J. Andrés, J. A. Varela and E. Longo, *Theor. Chem. Acc.*, 2009, **124**, 385–394.
- 35 R. C. Lima, L. R. Macario, J. W. M. Espinosa, V. M. Longo, R. Erlo, N. L. Marana, J. R. Sambrano, M. L. dos Santos, A. P. Moura, P. S. Pizani, J. Andrés, E. Longo and J. A. Varela, *J. Phys. Chem. A*, 2008, **112**, 8970–8978.
- 36 B. T. Collins and M. Ling, *J. Electrochem. Soc.*, 1993, **140**, 1752.
- 37 C. R. Wang, K. B. Tang, Q. Yang, C. H. An, B. Hai, G. Z. Shen and Y. T. Qian, *Chem. Phys. Lett.*, 2002, **351**, 385–390.
- 38 H. Luo, R. G. Greene, K. Ghandehari, T. Li and A. L. Ruoff, *Phys. Rev. B: Condens. Matter Mater. Phys.*, 1994, **50**, 16232–16237.
- 39 P. Kubelka, *J. Opt. Soc. Am.*, 1948, **38**, 448–448.
- 40 M. L. Myrick, M. N. Simcock, M. Baranowski, H. Brooke, S. L. Morgan and J. N. McCutcheon, *Appl. Spectrosc. Rev.*, 2011, **46**, 140–165.
- 41 R. A. Smith, *Semiconductors*, London, 1978.
- 42 Y. Kaneko and T. Koda, *J. Cryst. Growth*, 1990, **86**, 72–78.
- 43 Z. Luo, H. Li, H. Shu, K. Wang, J. Xia and Y. Yan, *Cryst. Growth Des.*, 2008, **8**, 2275.
- 44 Y. V. B. de Santana, C. W. Raubach, M. M. Ferrer, F. La Porta, J. R. Sambrano, V. M. Longo, E. R. Leite and E. Longo, *J. Appl. Phys.*, 2011, **110**, 123507.
- 45 V. M. Longo, L. Gracia, D. G. Stroppa, L. S. Cavalcante, M. Orlandi, A. J. Ramirez, E. R. Leite, J. Andres, A. Beltran, J. A. Varela and E. Longo, *J. Phys. Chem. C*, 2011, **115**, 20113–20119.
- 46 D. D. Jia, J. Zhu and B. Q. Wu, *J. Electrochem. Soc.*, 2000, **147**, 386–389.
- 47 V. Kumar, S. S. Pitale, V. Mishra, I. M. Nagpure, M. M. Biggs, O. M. Ntwaeaborwa and H. C. Swart, *J. Alloys Compd.*, 2010, **492**, L8–L12.
- 48 F. A. La Porta, M. M. Ferrer, Y. V. B. de Santana, C. W. Raubach, V. M. Longo, J. R. Sambrano, E. Longo, J. Andres, M. S. Li and J. A. Varela, *J. Alloys Compd.*, 2013, **556**, 153–159.
- 49 F. A. La Porta, M. M. Ferrer, Y. V. B. Santana, C. W. Raubach, V. M. Longo, J. R. Sambrano, E. Longo, J. Andrés, M. S. Li and J. A. Varela, *Curr. Phys. Chem.*, 2013, **3**(4), 378–385.